Title

Rapid and Energy-Efficient Synthesis of Disordered Rocksalt Cathodes

Journal

Advanced Energy Materials, 13(10)

ISSN

1614-6832

Authors

Wu, Vincent C
Evans, Hayden A
Giovine, Raynald
et al.

Publication Date

2023-03-01

DOI

10.1002/aenm.202203860

Rapid and Energy-Efficient Synthesis of Disordered Rocksalt Cathodes

*Vincent C. Wu Hayden A. Evans Raynald Giovine Molleigh B. Preefer Julia Ong Eric Yoshida Pierre-Etienne Cabelguen Raphaële J. Clément**

R. J. Clément
Materials Department and Materials Research Laboratory
University of California Santa Barbara, CA 93106, USA
Email Address: rclement@ucsb.edu
V. C. Wu, R. Giovine, J. Ong, E. Yoshida
Materials Department and Materials Research Laboratory
University of California Santa Barbara, CA 93106, USA
H. A. Evans
Center for Neutron Research
National Institute of Standards and Technology, Gaithersburg, MD 20899, USA
M. Preefer
Stanford Synchrotron Radiation Lightsource, SLAC
National Accelerator Laboratory, Menlo Park, CA 94025, USA
P.-E. Cabelguen
Umicore, New Business Incubation
31 rue du Marais, Brussels, 1000, Belgium

Keywords: *cation, disordered rocksalts, lithium-ion batteries, microwave synthesis*

Microwave heating enables the rapid and energy-efficient synthesis of disordered rocksalt cathodes, holding promise for cost-effective manufacturing strategies and high-throughput screening of new Li-ion cathode chemistries.

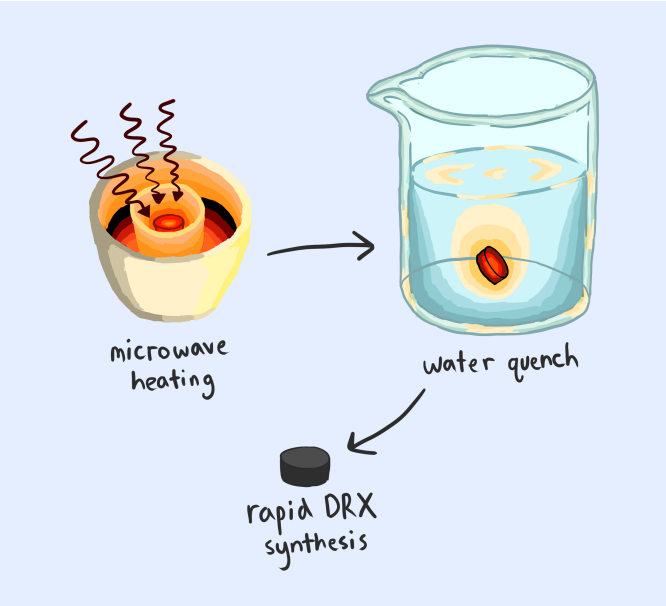

Lithium-rich transition metal oxides with a cation-disordered rocksalt structure (Disordered Rocksalt oXides or DRX) are promising candidates for sustainable, next-generation Li-ion cathodes due to their high energy densities and compositional flexibility, enabling Co- and Ni-free battery chemistries. However, current methods to synthesize DRX compounds require either high temperature (≈1000°C) sintering for several hours, or high energy ball milling for several days in an inert atmosphere. Both methods are time- and energy-intensive, limiting the scale up of DRX production. The present study reports the rapid synthesis of various DRX compositions in ambient air *via* a microwave-assisted solid-state technique resulting in reaction times as short as 5 minutes, which is more than two orders of magnitude faster than current synthesis methods. The DRX compounds synthesized *via* microwave are phase-pure and have a similar short- and long-range structure as compared to DRX materials synthesized *via* a standard solid-state route, resulting in nearly identical electrochemical performance. In some cases, microwave heating allows for better particle size and morphology control. Overall, the rapid and energy-efficient microwave technique provides a more sustainable route to produce DRX

materials, further incentivizes the development of next-generation DRX cathodes, and is key to accelerating their optimization *via* high-throughput studies.

1 Introduction

Lithium-ion batteries are energy dense, high power, and modular energy storage devices that play a pivotal role in grid storage applications and in the electrification of transportation. Currently, cathodes composed of layered transition metal oxides, such as lithium cobalt oxide (LCO)[1], lithium nickel cobalt manganese oxide (NMC)[2, 3], and lithium nickel cobalt aluminum oxide (NCA) [4] dominate the market due to their high energy densities and long cycle lives. However, those compounds contain redox-active cobalt (Co) and nickel (Ni) species that are expensive, toxic (in the case of Co), and whose resources are both geographically limited and mined in ethically questionable ways, resulting in complex and unreliable supply chains [5, 6, 7]. Thus, more sustainable cathode chemistries that still provide high energy densities are key to lowering the cost of Li-ion batteries. Li-excess Disordered Rocksalt oXides/ oXyfluorides (DRX) are a new class of energy-dense cathode materials whose redox activity is no longer tied to Co and Ni, and capacities in excess of 200 mAh/g have been reported for manganese (Mn)[8, 9, 10, 11]-, iron (Fe)[12, 8, 13, 14]-, and vanadium (V)[15, 16, 17]-based DRX cathodes. In particular, the DRX oxide $Li_{1.2}Mn_{0.4}Ti_{0.4}O_2$ displays a high energy density of >800 Wh/kg based on $Mn^{3+/4+}$ redox processes[9, 18, 19], while $Mn^{2+/4+}$ double redox has been achieved in the DRX oxyfluoride $Li_2Mn_{0.5}Ti_{0.5}O_2F$[20], resulting in an even higher energy density of >900 Wh/kg. However, when considering the large-scale implementation of these cathode materials, the energy demand associated with and the rate of materials production needs to be considered. For LCO, NMC, and NCA battery chemistries, most of the energy needed to produce a battery pack is spent on the synthesis and processing of the cathode material, largely due to the sustained heat input required for the co-precipitation and calcination steps[21, 22, 23]. Currently, DRX cathode materials are prepared using a high temperature (≈1000°C) anneal for around 12 hours under an Ar gas flow[24, 25, 26, 27], or *via* mechanochemical milling of precursor powders for several days in an Ar-filled jar[20, 16, 28, 29]. Both techniques require inert conditions and are time and energy intensive, and mechanochemical synthesis is difficult to scale, necessitating the development of faster and more sustainable methods to synthesize DRX compounds.

We demonstrate here a new method to synthesize DRX compounds under ambient air conditions via a microwave-assisted heating technique. This new heating method results in phase-pure DRX compounds in ≈5 minutes, a decrease in reaction time of more than two orders of magnitude compared to traditional furnace sintering, as well as commensurate energy savings since microwaves and furnaces operate at similar power levels (700 - 800 W). Two different compositions, $Li_{1.2}Mn_{0.4}Ti_{0.4}O_2$ and $Li_{1.3}Mn_{0.4}Nb_{0.3}O_{1-x}F_x$, were successfully synthesized via microwave-assisted processes, demonstrating the applicability of this method to the synthesis of a variety of DRX chemistries. The structure and properties of DRX cathode materials produced *via* this new microwave route were compared to those of compositional analogues obtained through high temperature sintering. Specifically, the morphology of the cathode particles, and the purity, composition, short-range structure, and electronic structure of the DRX phases, were examined. The electrochemical performance of the resulting DRX cathode composites was compared using galvanostatic charge-discharge cycling, differential capacity analysis, and rate tests. Overall, the newly developed microwave-assisted synthesis method provides significant time, energy and cost savings, while producing DRX cathode materials with similar atomic arrangements and performance to those obtained *via* more traditional solid-state methods. Importantly, this efficient synthetic route to DRX materials enables high throughput screening of new DRX chemistries and constitutes a leap forward in the realization of sustainable, cost-effective manufacturing strategies to support their deployment.

2 Microwave synthesis of DRX materials

Microwave-assisted solid-state synthesis of inorganic compounds utilizes microwave radiation to efficiently and rapidly heat and elicit reactions between the precursor powders.[30] In a typical setup, activated carbon is used as a susceptor that strongly couples to microwaves at room temperature and allows initial heating of the precursor powders via conductive and radiative heat transfer processes. Past a critical temperature, the precursors become directly susceptible to microwave radiation and rapidly heat from the core of the particles (as opposed to conductive heating that propagates from the surface to the core of the particles), allowing for rapid interdiffusion of species and formation of the final product.[30] The reported advantages of microwave heating over traditional furnace heating include extremely fast temperature ramp rates, higher achievable temperatures ($> 1500°C$), and reaction times on the order of minutes. Cumulatively, these advantages provide significant time and energy savings. Furthermore, the unique thermodynamics and kinetics of microwave synthesis may allow for the formation of metastable phases and particle morphologies that cannot be achieved through traditional solid-state methods [31].
We posit that DRX oxides can be formed via rapid, high temperature microwave heating. While entropically stabilized at elevated temperatures, DRX compounds are metastable at room temperature due to the significant ionic size differences between the transition metal and Li species occupying the octahedral interstices of the rocksalt oxide framework. Such size differences result in local structure distortions to accommodate the edge-sharing LiO_6 and transition metal-based MO_6 octahedra. Hence, at low temperature, ordered phases including the layered α-$LiFeO_2$ and spinel structure types are preferred, where Li and transition metal species are either spatially segregated or corner-sharing and the energy penalty from octahedral distortions is minimized.[32] However, in a microwave process where (1) high temperatures exceeding standard furnace capabilities can quickly be reached, and (2) the setup allows for rapid quenching of the product (a pellet can be removed from the hot crucible in less than 3 seconds), metastable DRX phases may be synthesized and stabilized down to room temperature.
We find that the successful synthesis of DRX compounds via a microwave route requires several additional experimental considerations. Initially, synthesis of the pure oxide $Li_{1.2}Mn_{0.4}Ti_{0.4}O_2$ was attempted through microwave heating of a hand-ground pelletized mixture of Li_2CO_3, Mn_2O_3, and TiO_2. Pellets were quenched in air after microwave irradiation, and various reaction times (from 5 to 40 minutes) were trialed. In all attempts, although the DRX phase was formed, a significant amount of ordered oxide impurities were also present, resulting in a product that was only around 60 to 70% phase-pure (Figure S1). We identified two possible causes for these impurity phases. First, although high temperatures are quickly achieved (crucibles become red-hot within 2-3 minutes), incomplete interdiffusion of species between the precursor powders may lead to only partial formation of the DRX structure. Second, while the cooling process is relatively fast, it is not instantaneous and the DRX likely has sufficient time to convert to an ordered phase upon cooling. In fact, the color of the pellet changed from black (DRX phase) to red (ordered oxide phase) during the air cooling process, and upon breaking the pellet in half the red ordered phase was largely observed as an outer layer whereas the center of the pellet remained mostly black. Those observations indicate the formation of impurities on the outside of the pellet, presumably due to exposure to an oxidative air environment, which in conjunction with a slow cooling process favors formation of ordered transition metal oxide phases.
To address the limitations mentioned above, the microwave-assisted synthesis protocol was modified. Fluorine in the form of LiF was added in small amounts (5% fluorination) to the precursor mix. Due to their small size, fluoride ions readily diffuse through crystalline frameworks and fluorine-containing compounds are often used as sintering agents in solid-state reactions, lowering the energy barriers associated with the diffusion of other species and rendering the precursor powders more reactive.[33, 34, 35] To resolve the issue of ordered oxide impurity phases forming during cooling in air, pellets were quenched in water instead. A schematic for this modified synthesis process is shown in Figure 1. With these improvements, we were able to successfully synthesize phase-pure $Li_{1.2}Mn_{0.4}Ti_{0.4}O_2$ (mw-LMTO) in 5 minutes (Figure 2a). We note that the use of both LiF as a sintering agent and a fast water quench is necessary to obtain phase-pure DRX compounds, as implementing only one of these two modifications resulted in significant impurity phases (Figure S2). A detailed description of the synthesis procedure can be found

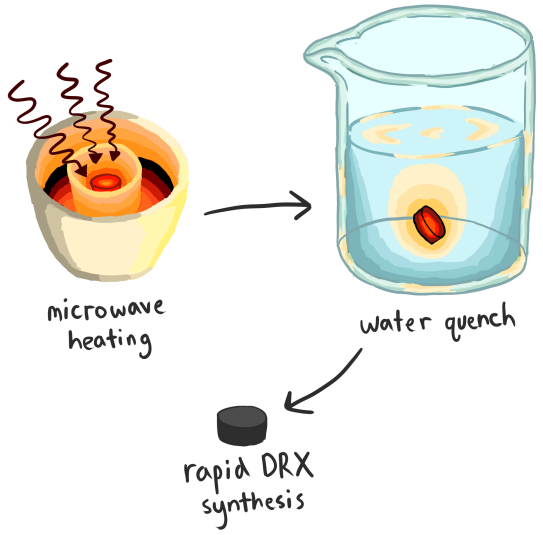

Figure 1: Schematic of microwave irradiation and water quenching process to synthesize DRX cathodes.

in the Experimental section. Overall, successful synthesis of phase-pure DRX compounds *via* microwave heating depends on the ability to reach sufficiently high temperatures while avoiding melting of the precursors, the use of a sintering agent (here, LiF) to facilitate species interdiffusion, and on a fast quenching process in a liquid to prevent reaction of the surface of the pellet with air.

3 Comparing $Li_{1.2}Mn_{0.4}Ti_{0.4}O_2$ (LMTO) synthesized *via* microwave and solid-state

3.1 Structural characterization

LMTO DRX compounds synthesized using different microwave heating times from 5 to 20 minutes (mw-LMTO) were compared to a compositional analogue prepared *via* a traditional solid-state route with a 12 h sintering step (details in the Experimental section), referred to as ss-LMTO, to assess possible differences in structure, composition, and electrochemical performance. Synchrotron X-ray diffraction (sXRD) patterns obtained on the four samples of interest are shown in Figure 2a. For all samples, the pure DRX structure is observed, with no visible crystalline impurity peaks. Pawley fits indicate that the a lattice parameter of the average rock salt structure (cubic space group $Fm\bar{3}m$) are all very similar, in the range of 4.150 Å- 4.153 Å(Table S1). The full patterns and a representative fit are shown in Figure S3. The broad, low intensity reflection centered around $2\theta \approx 3.2^{\circ}$ is indicative of cation short-range order (SRO) in the DRX structure.[9, 36, 37] Despite much faster reaction times and a faster quench rate for the mw-LMTO samples compared to ss-LMTO, both of which have been reported to significantly reduce SRO in standard solid-state synthesis of DRX compounds,[37] the broad reflection is present in all of the patterns. This is likely due to the higher temperatures reached in microwave synthesis, resulting in SRO formation on a faster timescale as compared to solid-state methods. Cation ordering at the local scale is an important parameter for DRX, as previous studies have shown that the type and degree of SRO significantly impacts cathode performance[9, 36, 37]. To probe SRO in more detail, X-ray pair-distribution function (PDF) analysis was employed and will be discussed later.
The morphologies of the as-synthesized DRX particles were examined *via* scanning electron microscopy (SEM) (Figure S4). ss-LMTO particles have a significantly wider size distribution and more irregular shapes compared to mw-LMTO. In contrast, microwave synthesis produces particles that are relatively uniform in size and morphology. This is advantageous as particle morphology control is an important step towards the commercialization battery electrode materials, where particle size, size uniformity, and

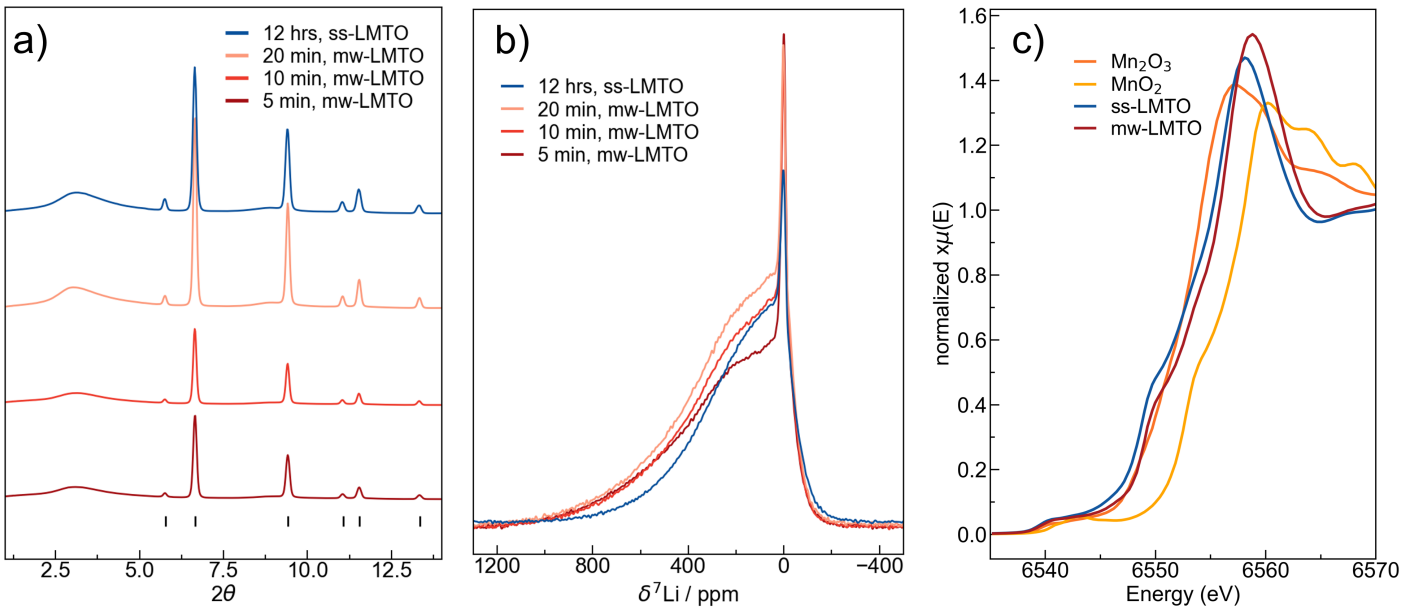

Figure 2: (a) Synchrotron XRD patterns ($\lambda = 0.24101$ Å) collected on LMTO DRX samples synthesized via microwave (mw) and solid-state (ss) with tick marks indicating expected Bragg peak positions for the $Fm\bar{3}m$ space group. (b) ^{7}Li pj-MATPASS solid-state NMR (ss-NMR) spectra collected on all LMTO samples. All spectra were acquired at 2.35 T with a magic angle spinning (MAS) speed of 60 kHz, and scaled according to the number of moles of Li in the rotor and the number of scans. (c) Mn K-edge XANES data collected on ss-LMTO and mw-LMTO, and on the Mn_2O_3 and MnO_2 reference samples.

morphology have been shown to influence the performance and long-term stability of cathodes.[38] As expected, the primary particle size increases with microwave heating time, from ≈ 1-2 μm at 5 minutes to ≈ 3-5 μm at 20 minutes.

3.2 Compositional analysis

To further examine the phase purity and stoichiometries of the synthesized LMTO products, we used a combination of inductively coupled plasma optical emission spectroscopy (ICP-OES), fluoride ion selective electrode (F-ISE) measurements, and solid-state NMR (ss-NMR). While ICP and F-ISE measurements can provide elemental ratios between Li, Mn, Ti, and F in the overall product powder, they do not provide any phase information and the actual DRX composition remains unknown, particularly since impurity phases are oftentimes amorphous and thus XRD-invisible. In contrast, ^{7}Li ss-NMR probes Li local environments in the sample in a quantitative manner and does not require the presence of long-range crystalline order. In this way, the molar amount of Li in potential impurity phases and in the DRX can be determined from ss-NMR, making it a powerful complementary technique to ICP and F-ISE. When it comes to assessing the possible integration of fluorine species into the rock salt oxide framework, one cannot rely on X-ray and neutron diffraction tools because of the very similar form factors/scattering lengths of fluorine and oxygen, rendering those two elements indistinguishable. There, ^{19}F ss-NMR provides direct insights into F local environments in the DRX and in potential impurity phases. Altogether, ICP, F-ISE, and ss-NMR can be used to estimate the purity and stoichiometry of the DRX phase. ^{7}Li ss-NMR spectra collected on the as-prepared mw- and ss-LMTO samples are compared in Figure 2b. The spectra were recorded using the projected magic angle turning phase-adjusted sideband separation (pj-MATPASS) pulse sequence, which removes spinning sidebands due to magic angle spinning (MAS) of the sample during data acquisition, and produces an isotropic ^{7}Li ss-NMR spectrum with minimal signal overlap, facilitating data interpretation. All spectra feature two distinct components: a broad, asymmetric signal corresponding to a distribution of Li environments in the DRX phase, which accounts for the majority of the signal intensity, and a sharp signal centered at ≈0 ppm that is attributed to diamagnetic

Sample	Li	DRX Li	Mn	Ti	F	% Li impurity
mw-LMTO, 5 min	1.310	1.14	0.4	0.392	0.055	12.6
mw-LMTO, 10 min	1.277	1.14	0.4	0.391	0.042	10.5
mw-LMTO, 20 min	1.278	1.15	0.4	0.394	0.032	9.8
ss-LMTO, 12 hr	1.277	1.15	0.4	0.398	0.001	9.8

Table 1: DRX stoichiometries obtained from ICP, F-ISE, and ^{7}Li ss-NMR for the as-prepared mw- and ss-LMTO samples, normalized to Mn. % Li impurity corresponds to the Li molar fraction contained within diamagnetic impurity phases. DRX Li refers to Li in the DRX phase, and was obtained by reducing the bulk Li measured *via* ICP by the amount of impurities determined through ^{7}Li ss-NMR. All other columns refer to the bulk elemental contents in the samples.

Li impurities such as Li_2CO_3, Li_2O, and LiF.[39] Li species in the DRX LMTO phases are surrounded by paramagnetic Mn^{3+} ions, resulting in strong hyperfine interactions between the unpaired electron spins and the Li nuclear spins and leading to significant broadening of the ^{7}Li NMR lineshapes and large Fermi contact shifts of the ^{7}Li resonant frequency. The magnitude and sign of Fermi contact shifts depend on the net unpaired electron spin density delocalized from the Mn *d* orbitals to the Li *s* orbitals through bonds, and therefore on the number of nearby paramagnetic Mn^{3+} ions ($<\sim$5Å from the Li nucleus) and on the Mn-O-Li bond pathway geometries. A disordered DRX structure with a large number of possible Li environments leads to a correspondingly large number of broad and overlapping resonances centered at various Fermi contact shifts, which altogether result in a broad, asymmetric signal in the ss-NMR spectrum. In contrast, Li in diamagnetic impurity phases do not experience significant broadening nor a shift of the resonant frequency and thus result in sharp resonances near 0 ppm. Given the large differences between paramagnetic and diamagnetic NMR lineshapes, fits and integration of fully relaxed ^{7}Li ss-NMR spin-echo spectra (not shown here) allow us to determine the fraction of Li in the DRX and in diamagnetic impurity phases in each sample, reported in Table 1. Further details on the quantification method can be found in Supplementary Note 1 and Figure S5.

The DRX stoichiometries for the four samples of interest, determined by combining the ICP, F-ISE, and ^{7}Li NMR results and by fixing the Mn content to its targeted value, are listed in Table 1. Since Li is volatile, a 10% Li molar excess was systematically added to the precursor mixtures, leading to a Li stoichiometry of 1.32 prior to heating. After a 5-minute microwave heating process, the total amount of Li (including Li impurities) in the sample (1.31) remains close to its starting value, indicating that Li does not have time to be significantly vaporized. For longer microwave heating times, and for the 12-hour solid-state synthesis, the amount of Li in the samples decreases significantly but the Li content remains above the targeted value of 1.2. ^{7}Li NMR results indicate that the molar fraction of Li in diamagnetic impurity phases decreases as the microwave time increases, and the mw-LMTO sample obtained after 20 minutes of microwave heating has the same impurity content as the ss-LMTO sample. Combining the ICP and NMR results, we find that the Li stoichiometry of the DRX phase is approximately the same for all of the samples, with a value in the range of 1.14-1.15. Thus, particularly for the 5-minute microwave heating process where Li does not vaporize significantly, Li excess is not needed and likely detrimental to the electrochemical performance of the product cathode powder, as Li that is not incorporated into the DRX phase forms impurities instead.

As mentioned earlier, small amounts of fluorine (in the form of LiF) were added to the precursor mixture to promote DRX formation during microwave heating (no sintering agent was used in the standard solid-state synthesis), and F-ISE and ^{19}F ss-NMR were used to determine whether fluorine had integrated the mw-LMTO structure. It is worth noting that partial fluorine substitution for oxygen has been found to enhance the structural stability of DRX cathode and improve their electrochemical performance.[20, 24, 40, 41] As shown in Table 1, the overall fluorine content in the sample, as determined from F-ISE measurements, decreases rapidly with increasing microwave heating time due to vaporization. After 5 minutes of microwave heating, half of the fluorine present in the precursor mixture has been lost. Semi-quantitative fits of the ^{19}F ss-NMR spectra collected on the mw-LMTO samples (Figure S6) indicate that $\approx$40% of the fluorine present in the 5 minute mw-LMTO sample is in the form of LiF. Further analysis, detailed in Supplementary Note 2, provides an upper limit of $\approx$2.4% fluorination for the DRX LMTO

phases prepared by microwave heating, a very small amount that enables us to compare them to the ss-LMTO (pure oxide) cathode.

3.3 Local and electronic structure

Mn K-edge X-ray absorption spectroscopy (XAS) was used to determine the average oxidation state of Mn in the mw-LMTO and ss-LMTO samples. It is clear from the X-ray absorption near edge structure (XANES) spectra shown in Figure 2c that the Mn K-edge energies recorded for the mw-LMTO samples are higher than those measured for the ss-LMTO sample, indicating a higher average Mn oxidation state in the former samples. Although it is difficult to extract absolute oxidation states from those measurements given that no disordered oxide reference compound exists to date,[24] the relatively minor edge energy shifts relative to the limits set by the Mn_2O_3 (Mn^{3+}) and MnO_2 (Mn^{4+}) references suggest that Mn is still mostly in the 3+ oxidation state in the microwaved samples. We attribute those results to the different atmospheric environments used in the microwave and solid-state syntheses, whereby the microwave syntheses were performed in ambient air, a more oxidizing environment than the Ar atmosphere used in the solid-state synthesis.

To obtain additional insights into the type and extent of cation SRO in the DRX compounds of interest, leading to the broad, low angle reflection in the sXRD data (Figure 2a), X-ray PDF analysis was conducted on the 5 minute mw-LMTO and ss-LMTO samples. Refinements of the PDF data over several ranges of correlation lengths r are shown in Figure 3. Three different structural models were used to fit the data: a cubic rock salt model corresponding to a random distribution of cations (space group $Fm\bar{3}m$, #255), and two tetragonal models corresponding to spinel-like and γ-$LiFeO_2$-like cation ordered structures (space group I41/amd, #141). For both mw-LMTO and ss-LMTO, the cubic rock salt model best describes the data at long correlation lengths (in the range of 5 Å to 30 Å), consistent with the sXRD results. PDF analysis reveals, however, that the cubic model is inappropriate to describe the mw-LMTO and ss-LMTO DRX structures at very local correlation lengths (1.6 Å to 3.2 Å), as it is unable to reproduce the two correlation peaks at 2.0 Å and 2.4 Å(see Figure 3). On the other hand, the spinel-like and γ-$LiFeO_2$-like structural models allow for oxygen atomic displacements and can therefore account for those peaks, with the spinel-like structural model providing the best fit of the data, as shown in Figure S7. The parameters used in the fits are described in more detail in Supplementary Note 3, where we also explain why the impurity phases detected by ss-NMR minimally impact the PDF results. Briefly, the tetragonal models exhibit two crystallographic cation sites with Li/Mn/Ti occupancies that can be refined using constraints on the metal ratios obtained from ICP. Using either of those two models, the ss-LMTO and mw-LMTO local structures are best described by ordering the transition metals on one of the two allowed cation sites, and with Li species occupying the other cation site. In the mid-range region, the PDF data is best fit when the transition metal and Li species are equally distributed over the two cation sites.

Overall, out of the three models considered here, the spinel-like cation-ordered model best fits the short-range correlations. However, it is not possible to ascertain whether the local structure is truly spinel-like given the limited number of cation orderings and the small range of correlation lengths considered here. Importantly, the cubic and tetragonal models produce chemically similar fits of the PDF data obtained on mw-LMTO and ss-LMTO in the mid-range region (2 Å to 7 Å), and our analysis suggests a comparable degree of short-range ordering in both of these long-range disordered samples.

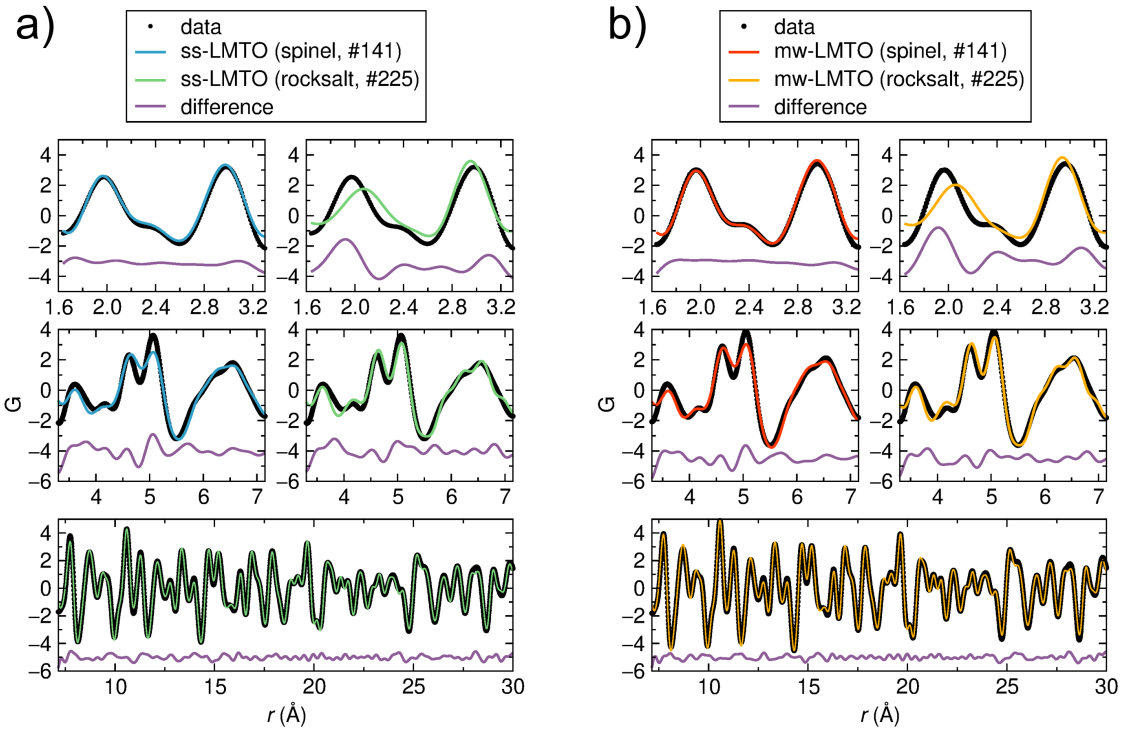

Figure 3: Fits of the x-ray PDF data collected on (a) ss-LMTO and (b) mw-LMTO obtained with a 5 minute microwave heating step. The PDF datasets are fit at short, medium, and long correlation lengths using a cubic rocksalt model (space group $Fm\bar{3}m$, #255) and a spinel tetragonal model (space group I41/amd, #141). The cation-ordered spinel-like model is shown in Figure S8.

3.4 Electrochemical performance

The electrochemical properties of ss-LMTO and 5 minute mw-LMTO were compared in Li half cells. As a first step, the pristine DRX powders were mechanochemically mixed with Super C65 to introduce conductive carbon into the cathode composite and reduce particle size, enhancing the electronic and ionic conductivity of the electrode. SEM images of the processed LMTO samples are shown in Figure S4b and reveal the presence of primary particles of about 100 nm in size in both samples. Half cells composed of a DRX composite cathode, a standard Li electrolyte, and a Li metal anode were galvanostatically charged/discharged at room temperature at a rate of 20 mA/g for 50 cycles. Since the purpose of these tests is simply to compare the electrochemical performance of the DRX cathodes, rather than maximize capacity or rate performance, no further electrode and electrolyte optimization was conducted. The resulting voltage profiles for mw-LMTO and ss-LMTO, shown in Figure 4a-b, are quite similar. Both exhibit initial and final discharge capacities of ≈200 mAh/g and ≈130 mAh/g, respectively, corresponding to energy densities of ≈600 Wh/kg and ≈320 Wh/kg. 35% capacity fade and an average coulombic efficiency of 98% are observed over the first 50 cycles for both samples (Figure 4d). The evolution of the cell's voltage with cycling is identical for the two materials, with an average discharge potential fading from 3.1 V to 2.6 V vs. Li/Li^+, and an average charge potential stable at around 3.7 V for the first 50 cycles. The open-circuit voltage (OCV) of mw-LMTO is slightly higher than that of ss-LMTO (2.8 V vs. 2.5 V), consistent with the higher average Mn oxidation state observed for the former compound by XAS. To identify the redox processes taking place in the DRX cathodes of interest, differential capacity analysis (Figure 4c) was conducted. dQ/dV curves for mw-LMTO are consistent with previous reports on this DRX composition [42, 19], where the first peak at ≈3.6V in the initial charge corresponds to Mn^{3+}-Mn^{4+} oxidation, and the second higher voltage process at ≈4.5V corresponds to oxygen-based oxidation processes accompanied by irreversible side reactions. On discharge, the corresponding oxygen-based reduction process occurs at a slightly lower voltage and contributes to the voltage hysteresis observed during galvanostatic cycling, while Mn^{4+}-Mn^{3+} reduction occurs at 3.4 V. In subsequent cy-

cles, the Mn oxidation peak shifts to a lower voltage of 3.4 V, and the high voltage process is reduced in intensity and becomes fully reversible, although the voltage hysteresis is still present. A small difference between the dQ/dV profiles of the mw-LMTO and ss-LMTO cathodes is noted in the high voltage charging regime, where the oxygen-based redox peak is shifted to slightly higher potentials for the mw-LMTO cathode.

Variable rate cycling tests were also performed and the results are shown in Figure 4e. The similar DRX particle size distributions in the ss-LMTO and mw-LMTO samples, and the similar cathode film loading densities used for cell assembly, allow us to eliminate those two factors known to affect rate performance. The ss-LMTO cathode performs better than the mw-LMTO cathode at the higher current densities tested here (100 mA/g and above). Since both the short- and long-range structure of the mw-LMTO and ss-LMTO phases are almost identical, as evidenced by sXRD and PDF analysis, the disparity in rate performance may be due to the greater amount of impurities, such as Li_2CO_3, in the mw-LMTO sample (as observed by ss-NMR), or to surface reconstruction upon exposure to water during quenching. Thus, further fine-tuning of the microwave synthesis procedure to reduce side products will likely improve high-rate cycling of mw-LMTO. Overall, the electrochemical properties of mw-LMTO are very similar to those of ss-LMTO, indicating that the microwave synthesis process can produce highly performing DRX cathode materials.

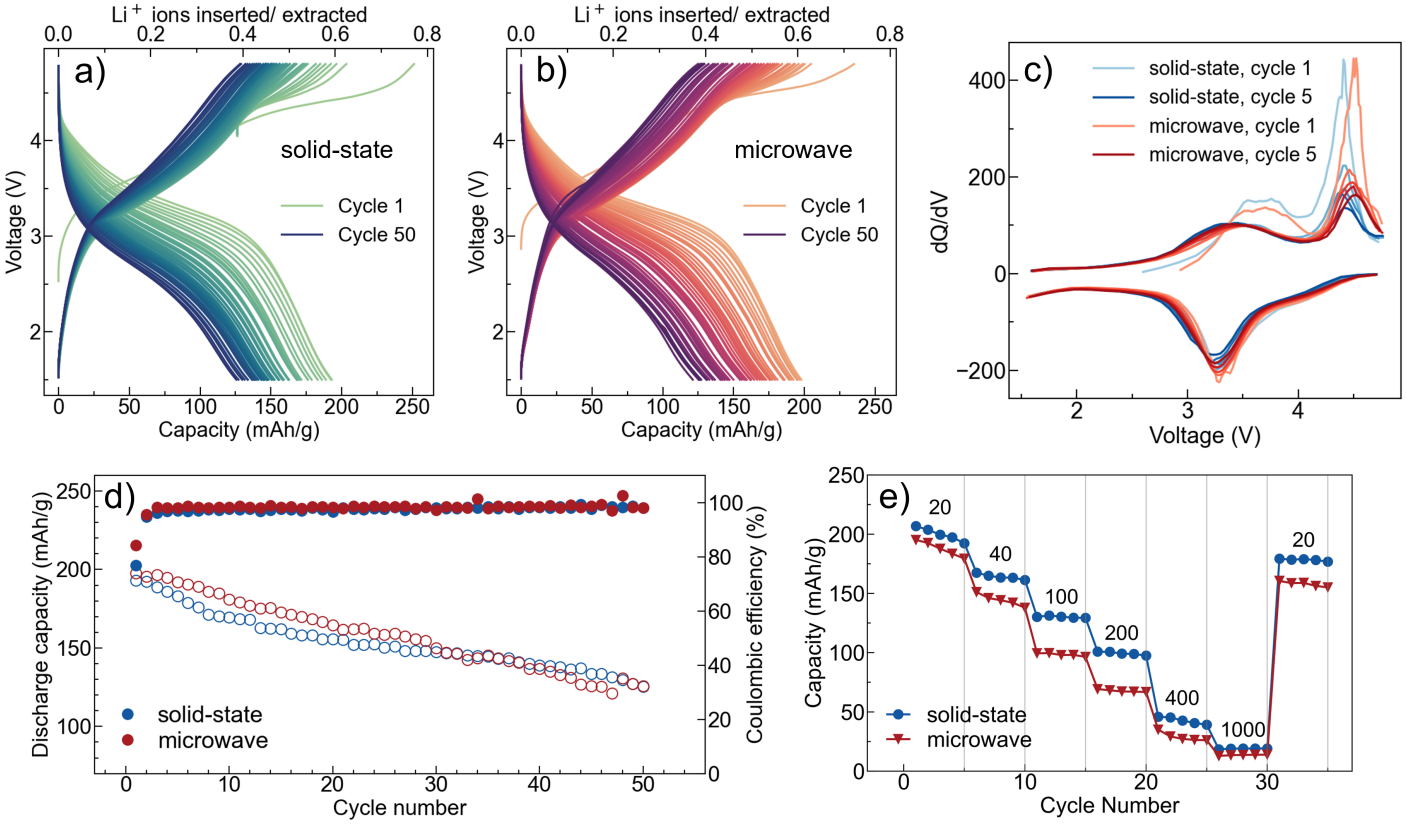

Figure 4: Voltage vs. capacity plots obtained during galvanostatic cycling of LMTO synthesized via (a) solid-state (ss-LMTO) and (b) microwave (mw-LMTO) methods. (c) Differential capacity plots obtained during the first five cycles. (d) Evolution of the discharge capacity and coulombic efficiency of the ss-LMTO and mw-LMTO cathodes over the first 50 cycles, where open and closed markers denote capacity and coulombic efficiency, respectively. (e) Rate capacities of the ss-LMTO and mw-LMTO cathodes, with rate value displayed on the graph in units of mA/g.

4 Structure and performance of $Li_{1.3}Mn_{0.4}Nb_{0.3}O_{2-x}F_x$ synthesized *via* microwave

4.1 Synthesis and structural characterization

To demonstrate the broader applicability of our newly-developed microwave heating method for the synthesis of DRX oxides and oxyfluorides, we explored the $Li_{1.3}Mn_{0.4}Nb_{0.3}O_{2-x}F_x$ compositional series, where Nb replaces Ti as the structure-stabilizing, high-valent d^0 transition metal. $Li_{1.3}Mn_{0.4}Nb_{0.3}O_{2-x}F_x$ compounds prepared *via* microwave and solid-state routes are hereafter referred to as mw-LMNO/F and ss-LMNO, respectively. As with mw-LMTO, a small excess of fluorine in the form of LiF was added to the precursor mix (equivalent to 5% fluorination) to prepare mw-LMNO/F, while the pure oxide (x = 0) was targeted for the solid-state route. Unlike mw-LMTO, however, a stoichiometric Li content was used instead of a 10% Li excess to prepare the mw-LMNO/F compounds, since little volatility was observed in the synthesis of LMTO (Table 1). Further details on the synthesis of mw-LMNO/F and ss-LMNO can be found in the Experimental section.

sXRD results, shown in Figure 5a, suggest the formation of pure ss-LMNO and mw-LMNO/F DRX phases obtained using microwave heating times of 5, 10, and 20 minutes (full sXRD patterns and a representative Pawley fit are shown in Figure S3). Pawley refinements of the sXRD data yield very similar lattice parameters for all of the samples, in the range of 4.195-4.202 Å (Table S1). The broad reflections centered around $2\theta \approx 3.5^\circ$ and 8.75° ($\lambda = 0.24101$ Å) are once again indicative of SRO in the DRX structures. X-ray PDF analysis was performed on ss-LMNO and 5 minute mw-LMNO/F, and refinements were conducted using the same cubic and tetragonal models as those used previously for LMTO. A similar type of SRO is identified for the two DRX structures (Figures S9-10), with fits indicating that, at very local correlation lengths (1.6 Å to 3.2 Å), cation ordered tetragonal models are more appropriate descriptions of the structure, and at long-range correlation lengths (>5 Å) the cubic rock salt model is more appropriate. SEM images further reveal that increasing the microwave reaction time increases the average particle size from 1-5 μm at 5 minutes to ≈10 μm at 20 minutes (Figure S11).

As with LMTO, the broad, asymmetric signal observed in the ^{7}Li ss-NMR spectra collected on the LMNO/F samples (Figure 5b) corresponds to the DRX Li environments, while the sharp signal near 0 ppm arises from Li in diamagnetic impurity phases (e.g., Li_2CO_3, Li_2O, and LiF). The molar fraction of Li in diamagnetic impurity phases in each sample, obtained from fits and integration of the ^{7}Li ss-NMR spectra and listed in Table S2, once again indicates a decrease in the amount of diamagnetic impurities as the microwave heating time increases, reaching a value of 15-16% for the 20 minute mw-LMNO and ss-LMNO samples. Despite the use of stoichiometric amounts of Li, the mw-LMNO/F and ss-LMNO samples contain more impurities than the LMTO samples. We note, however, that the molar fractions of Li in diamagnetic impurity phases reported in this work are on par with those reported in previous ^{7}Li ss-NMR studies on similar DRX compositions [20, 43, 10, 44] (many more studies do not include ^{7}Li ss-NMR data and therefore do not report accurate stoichiometries for the DRX phases under scrutiny).

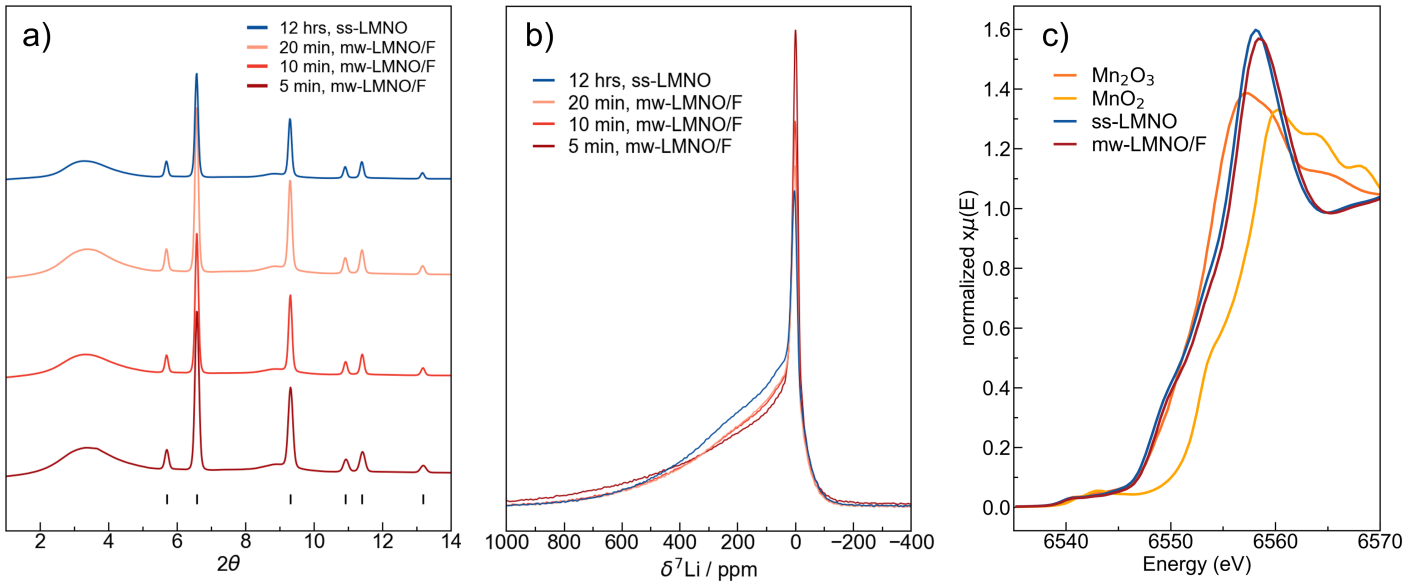

Figure 5: (a) Synchrotron XRD patterns ($\lambda = 0.24101$ Å) and (b) ^{7}Li pj-MATPASS ss-NMR spectra collected on ss-LMNO and mw-LMNO/F samples with tick marks indicating the expected Bragg peak positions for the Fm$\bar{3}$m space group. All NMR spectra were acquired at 2.35 T with a MAS speed of 60 kHz, and were scaled according to the number of moles of Li/F in the rotor and the number of scans. (c) Mn K-edge XANES of ss-LMNO and mw-LMNO/F along with Mn_2O_3 and MnO_2 reference samples.

^{19}F ss-NMR spectra collected on the 5, 10, and 20 minute mw-LMNO/F samples, along with the 5 minute mw-LMTO sample, are shown in Figure S12. Unlike mw-LMTO, no LiF is detected in any of the mw-LMNO/F samples (Figure S12b). The higher intensity of the ^{19}F ss-NMR signals obtained from the DRX mw-LMNO/F phases, in comparison to the DRX signal obtained from the mw-LMTO reference sample, indicates more significant fluorination of the Nb-containing DRX phases. This result is to be expected from the higher Li content in LMNO/F (1.3) vs. LMTO (1.2), and the strong preference of F to incorporate into Li-rich local environments in DRX oxides [45, 24, 28]. While we could not analyze the LMNO samples with ICP due to the difficulty of digesting Nb-containing samples, and we could therefore not obtain the exact fluorination level of the DRX phases, it is clear from the decrease in the overall ^{19}F signal intensity going from the 5 minute to the 20 minute mw-LMNO/F sample that the fluorine content in the mw-LMNO/F phase decreases with longer microwave times.
Finally, the average Mn oxidation state of the mw-LMNO/F samples is slightly higher than that of ss-LMNO, as revealed by the Mn K-edge XANES data shown in Figure 5c.

4.2 Electrochemical performance

The electrochemical properties of the 5 minute mw-LMNO/F and ss-LMNO cathodes were studied in Li half-cells. As with LMTO, the pristine DRX powders were first ball milled with Super C65, and the SEM images on the processed mw-LMNO/F and ss-LMNO samples, shown in Figure S11b, reveal the presence of primary particles of about 100 nm in size. As shown in Figures 6a-b, the solid-state and microwaved cathodes perform similarly, with initial and final discharge capacities of ≈270 mAh/g and ≈130 mAh/g, corresponding to energy densities of ≈850 Wh/kg and 330 Wh/kg, respectively. Although the first cycle capacity of LMNO/F is generally higher than that of LMTO, its capacity decay is also more severe and after 50 cycles the capacity retention is only of ≈50% (Figure 6d). The coulombic efficiency, average discharge potential, voltage hysteresis, and voltage fade are almost identical for the mw-LMNO/F and ss-LMNO cathodes. The OCV of the mw-LMNO/F cathode is slightly higher than that of ss-LMNO, indicating a higher average Mn oxidation state in the former, which is consistent with the Mn K-edge XANES results (Figure 5c). Differential capacity curves also exhibit standard DRX cathodic and anodic peak trends. At higher cycling rates, ss-LMNO performs better than mw-LMNO/F, which is most likely

due to the higher amount of impurities in the 5 minute mw-LMNO/F sample.

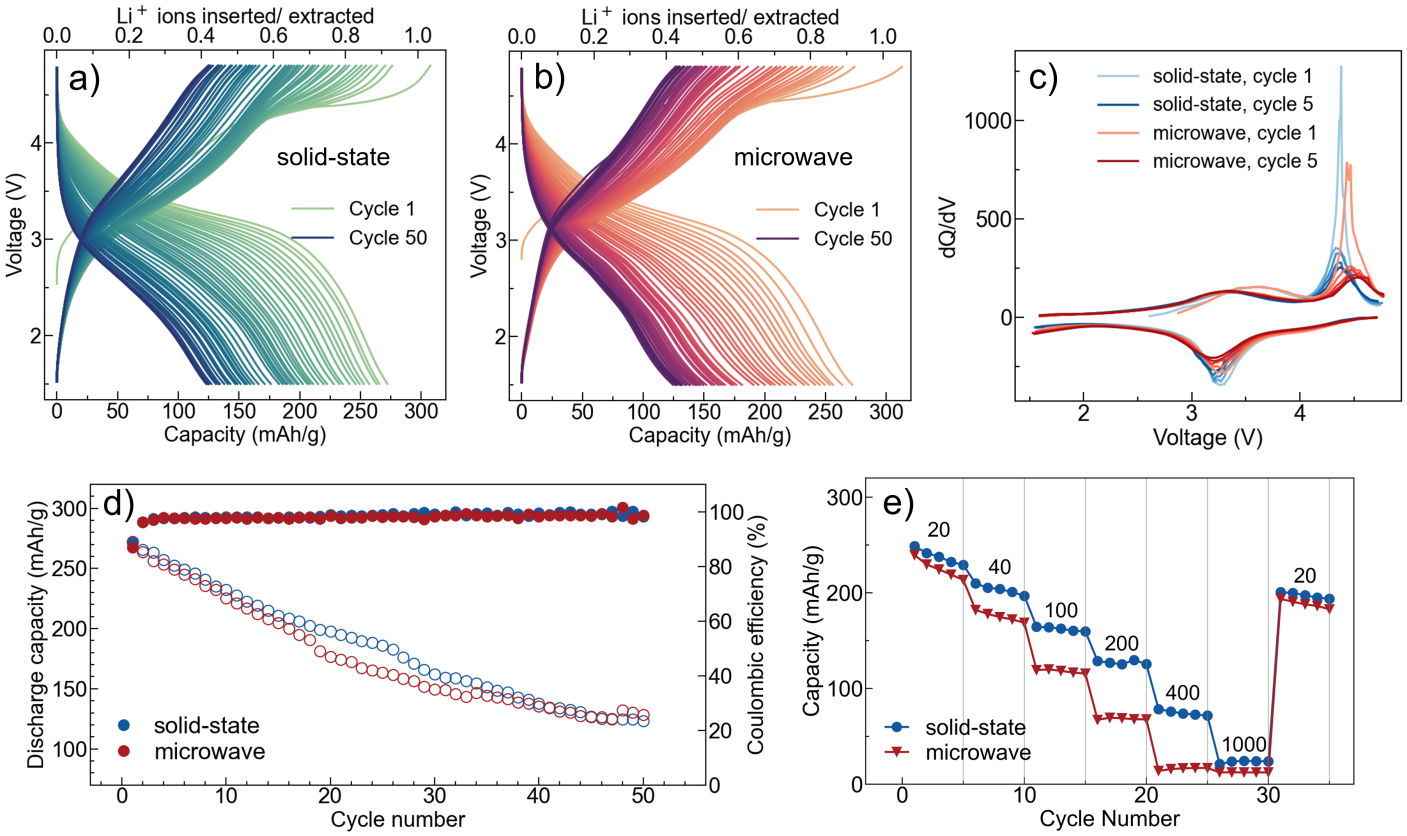

Figure 6: Galvanostatic cycling plots of LMNO/F synthesized via (a) solid-state and (b) microwave methods. (c) Differential capacity plots obtained during the first five cycles. (d) Evolution of the discharge capacity and coulombic efficiency of solid-state and MW LMNO/F DRX cathodes over 50 cycles, where open and closed markers denote capacity and coulombic efficiency, respectively. (e) Rate capacities of solid-state and MW LMNO/F DRX cathodes, with rate value displayed on the graph in units of mA/g.

Overall, the electrochemical performance of DRX cathodes prepared *via* microwave heating is on par with their compositional and structural analogues obtained via a standard solid-state route, except for their rate capability. We believe that the latter can be enhanced through further optimization of the microwave heating process and subsequent quenching step, to reduce the amount of Li-containing diamagnetic impurities that in turn lower the Li^+ and electronic conduction properties of the sample.
As mentioned earlier, fluorination of DRX oxide cathodes improves their electrochemical performance. Hence, further increasing the amount of fluorine that can be incorporated into the DRX oxide framework *via* microwave synthesis will be the focus of future work. While the present work already demonstrates a new rapid, energy- and cost-effective route towards DRX production, it is likely that this non-equilibrium synthesis method that allows rapid heating of the precursor mixture and quenching of the product will also provide opportunities for the preparation of novel DRX compositions that cannot be obtained through conventional solid-state routes.

5 Conclusion

We report herein a rapid, energy- and cost-effective method to prepare high energy density disordered rocksalt cathodes (DRX). This new microwave-assisted synthesis technique enables rapid, in-core heating of the precursor powders, and formation of phase pure DRX cathodes in 5 minutes in ambient air, providing significant time and energy savings compared to traditional solid-state and mechanochemical synthesis methods typically conducted in an inert atmosphere. The present microwave synthesis provides

a plethora of advantages, both in commercial and research settings. First, drastically reduced reaction times enable fast materials development cycles, which can expedite the deployment of high energy density, Co- and Ni- free DRX cathode chemistries. Second, the non-equilibrium microwave synthesis procedure described here uniquely combines extremely rapid heating with fast quenching of the pellet in water after microwave radiation, and holds promise for the preparation of a wider range of metastable DRX compositions. Third, for certain DRX compositions such as LMTO, microwave synthesis leads to more uniform particle sizes and morphologies; control of those parameters is central to the optimization of cathode material manufacturing processes.

To demonstrate the broad applicability of the microwave technique, we prepared and characterized two DRX compositional series, namely $Li_{1.2}Mn_{0.4}Ti_{0.4}O_2$ (LMTO) and $Li_{1.3}Mn_{0.4}Nb_{0.3}O_{2-x}F_x$ (LMNO/F). We find that DRX phase purity strongly improves with the addition of LiF as a sintering agent in the precursor mixture, and on the quenching rate after microwave radiation. A comparative analysis of LMTO and LMNO/F compounds obtained *via* microwave and solid-state synthesis indicates that the two synthesis methods can yield materials with very similar compositions, short- and long- range structures, and electrochemical performance. Those findings motivate the immediate replacement of energy-intensive and time-consuming solid-state and mechanochemical synthesis processes by greener and effective microwave-assisted routes for the preparation of next-generation DRX Li-ion battery cathodes.

6 Experimental

Microwave synthesis of mw-LMTO and mw-LMNO/F: For mw-LMTO, stoichiometric amounts of the Li_2CO_3, LiF, Mn_2O_3, and TiO_2 precursors were used with the target formula $Li_{1.32}Mn_{0.4}Ti_{0.4}O_{1.9}F_{0.1}$. 10% Li excess was used to compensate for possible Li loss during microwave heating. For mw-LMNO/F, stoichiometric amounts of the Li_2CO_3, LiF, Mn_2O_3, and Nb_2O_5 precursors were used with the target formula $Li_{1.3}Mn_{0.4}Nb_{0.3}O_{1.9}F_{0.1}$; no Li excess was used for mw-LMNO/F. Precursor powders were hand ground for 30 minutes and then pressed into 200 mg pellets. A double crucible setup was used for microwave synthesis, where a small alumina crucible was placed inside a larger crucible filled with 5 g of activated charcoal. The precursor pellet was placed in the small alumina crucible on top of a layer of sacrificial precursor powder to prevent reaction between the alumina surface and the pellet. The entire setup was placed in a conventional 1200W microwave, and heated at 60% power (720W) for 5, 10, or 20 minutes, under an ambient air atmosphere. Upon termination of microwaves, the pellet was immediately quenched into a beaker of distilled water to stabilize the DRX phase. The DRX pellet was then dried on a hot plate and ground into powder.

Solid-state synthesis of ss-LMTO and ss-LMNO: A standard solid-state synthesis protocol was used to synthesize ss-LMTO and ss-LMNO. For ss-LMTO, stoichiometric amounts of the Li_2CO_3, Mn_2O_3, and TiO_2 precursors were used with the target formula $Li_{1.32}Mn_{0.4}Ti_{0.4}O_2$. 10% Li excess was used to compensate for possible Li loss. For ss-LMNO, stoichiometric amounts of the Li_2CO_3, Mn_2O_3, and Nb_2O_5 precursors were used with the target formula $Li_{1.3}Mn_{0.4}Nb_{0.3}O_2$; no Li excess was used for ss-LMNO. Precursor powders were mixed via wet ball-milling with ethanol in a planetary ball-mill at 300 rpm (5 Hz) for 6 hours. The resulting slurry was dried to form a powder, and pressed into 200 mg pellets. The pellets were then heated at 1100°C (1373 K) for 12 hours under Ar gas flow, and allowed to naturally cool to room temperature.

Characterization: X-ray diffraction and pair distribution function measurements were performed on ≈40 mg samples at beamline 17-BM at the Advanced Photon Source at Argonne National Laboratory. All samples were measured at room temperature (≈303 K). Scattered intensity was measured by a Perkin Elmer amorphous-Si flat panel detector. The wavelength for the measurements was 0.24117 Å. The TOPAS software suite was used for Pawley refinements treatment of these data sets.[46] Pair distribution function g(r) data sets were obtained by reducing image files obtained from area detector at 17-BM to .chi files using GSAS II.[47] The .chi files were further transformed to g(r) data files using the xPDFsuite

software package [48] with a Q_{max} of 16.9 Å. Least-squares refinement of PDF data was performed using PDFGUI.[49] SEM images were obtained using a Thermo Fisher Apreo C LoVac SEM instrument with an accelerating voltage of 5 keV and current of 0.4 nA. Particle size analysis was carried out in ImageJ software [50]. Bulk chemical compositions were determined via ICP (Agilent 5800 ICP-OES) and fluoride selective ion electrode (Cole-Parmer) measurements. DRX samples were digested in a mixture of nitric acid and hydrochloric acid. For ICP, the digested solutions were diluted with distilled water. For F-ISE measurements, the solutions were diluted using a sodium acetate buffer and a fluoride ionic strength adjuster solution (TISAB, Cole-Parmer).

Solid-state nuclear magnetic resonance spectroscopy: Solid state ^{7}Li and ^{19}F NMR spectra were acquired at B_0 = 2.35 T (100 MHz for ^{1}H) using a wide bore Bruker BioSpin spectrometer equipped with a DMX 500 MHz console and a custom-made 1.3 mm single X-broadband magic angle spinning (MAS) probe tuned to ^{7}Li (38.9 MHz) or ^{19}F (94.1 MHz). Samples were loaded into 1.3 mm zirconia rotors and closed using Vespel caps. The samples were spun at the magic angle (MAS) at ν_R= 60 kHz using dry nitrogen. ^{7}Li and ^{19}F chemical shifts were externally referenced against 1M aqueous LiCl (^{7}Li $\delta_{iso} = 0$ ppm) and NaF (^{19}F $\delta_{iso} = -118.14$ ppm) solutions, respectively. Both ^{7}Li and ^{19}F MAS NMR spectra were obtained using a rotor synchronized spin-echo sequence (90° - τ_R - 180° - τ_R) with 90° radio frequency (RF) pulses of 0.45 μs and 0.30 μs, respectively. For ^{7}Li quantitative spin-echo spectra (τ_R = 1 rotor period), a total of 64 transients were averaged with a recycle delay of 20 sec which was enough to reach full relaxation of ^{7}Li signals. Fully relaxed ^{19}F NMR spectra were obtained with a recycle delay of 20 s and signals were averaged over 256 transients with a presaturation step resulting in an acquisition time of 1 h 25 min per sample. To enhance the signal-to-noise ratio of ^{19}F paramagnetic signals, a much shorter recycle delay of 50 ms was used which allowed a larger number of transients (131,072) to be acquired over a reasonable amount of time (2 h per sample). To reduce ^{19}F probe background signal, a T2 filter was used and consisted of increasing the wait time τ_R between the 90° and 180° pulse to 15 rotor periods. Solid-state NMR data were processed using Bruker TopSpin 3.6.0 and spectra were fit using DMfit software.[51]

X-ray absorption spectroscopy: X-ray absorption spectroscopy (XAS) was performed on beamline 4-1 at the Stanford Synchrotron Radiation Lightsource (SSRL) at SLAC National Accelerator Laboratory equipped with a double-crystal Si(220) monochromator, ϕ=90 degrees. Powder samples were adhered to kapton tape and mounted to slotted aluminum sample holders. The sample holders were positioned at a 45 degree angle to the incident X-ray beam, and fluorescence XAS data was collected at the Mn K-edge with a vertical beam size of 1 mm. The sweeps started at 6310 eV and ended at 7210 eV, repeated four times per sample. A Mn foil was measured simultaneously to reference correct the data. The data was processed using Athena (Demeter package).[52]

Electrochemistry: Electrochemical performance of DRX was tested in coin cells assembled in an Ar filled glovebox. DRX cathode films were produced by mixing the post-processed, carbon coated DRX powders with polytetrafluoroethylene (PTFE) such that the active material: carbon: binder ratio was 70:20:10. Films were then rolled out and punched to form 6.35 mm diameter discs with loading densities of 5-6 mg/cm^2. CR2023-type coin cells were assembled using the cathode film and a Li metal anode. 1M $LiPF_6$ in ethylene carbonate and dimethyl carbonate (EC/DMC with a 1:1 volume ratio) electrolyte was used, along with a Celgard 2325 separator.

Supporting Information

Supporting Information is available from the Wiley Online Library or from the author.

Acknowledgements

We thank Dr. Shinichi Kumakura and Dr. Violetta Arszelewska for stimulating discussions. This work was supported by Umicore. This work made use of the Spectroscopy, and Microscopy and Microanalysis shared facilities of the UC Santa Barbara MRSEC (DMR 720256), a member of the Materials Research Facilities Network (http://www.mrfn.org). Powder X-ray diffraction and Pair Distribution data were collected on beamline 17-BM at the Advanced Photon Source at Argonne National Laboratory, which is supported by the U.S. Department of Energy, Office of Science, Office of Basic Energy Sciences, under

Contract DEAC02-06CH11357. Use of the Stanford Synchrotron Radiation Lightsource, SLAC National Accelerator Laboratory, is supported by the U.S. Department of Energy, Office of Science, Office of Basic Energy Sciences under Contract No. DE-AC02-76SF00515. V.C.W. was supported by the NSF Graduate Research Fellowship under Grant No. DGE 1650114. Certain commercial equipment, instruments, or materials are identified in this document. Such identification does not imply recommendation or endorsement by the National Institute of Standards and Technology, nor does it imply that the products identified are necessarily the best available for the purpose.

References

[1] K. Mizushima, P. Jones, P. Wiseman, J. Goodenough, *Materials Research Bulletin* **1980**, *15*, 6 783.

[2] T. Ohzuku, Y. Makimura, *Chemistry Letters* **2001**, *30*, 7 642.

[3] H.-J. Noh, S. Youn, C. S. Yoon, Y.-K. Sun, *Journal of Power Sources* **2013**, *233* 121.

[4] M. Guilmard, *Solid State Ionics* **2003**, *160*, 1-2 39.

[5] E. A. Olivetti, G. Ceder, G. G. Gaustad, X. Fu, *Joule* **2017**, *1*, 2 229.

[6] C. Vaalma, D. Buchholz, M. Weil, S. Passerini, *Nature Reviews Materials* **2018**, *3*, 4 18013.

[7] K. Turcheniuk, D. Bondarev, G. G. Amatucci, G. Yushin, *Materials Today* **2021**, *42* 57.

[8] N. Yabuuchi, M. Takeuchi, M. Nakayama, H. Shiiba, M. Ogawa, K. Nakayama, T. Ohta, D. Endo, T. Ozaki, T. Inamasu, K. Sato, S. Komaba, *Proceedings of the National Academy of Sciences* **2015**, *112*, 25 7650.

[9] H. Ji, A. Urban, D. A. Kitchaev, D.-H. Kwon, N. Artrith, C. Ophus, W. Huang, Z. Cai, T. Shi, J. C. Kim, H. Kim, G. Ceder, *Nature Communications* **2019**, *10*, 1 592.

[10] Z. Lun, B. Ouyang, Z. Cai, R. J. Clément, D.-H. Kwon, J. Huang, J. K. Papp, M. Balasubramanian, Y. Tian, B. D. McCloskey, H. Ji, H. Kim, D. A. Kitchaev, G. Ceder, *Chem* **2020**, *6*, 1 153.

[11] K. Zhou, Y. Li, S. Zheng, M. Zhang, C. Zhang, C. Battaglia, H. Liu, K. Wang, P. Yan, J. Liu, Y. Yang, *Energy Storage Materials* **2021**, *43* 275.

[12] M. Tabuchi, A. Nakashima, H. Shigemura, K. Ado, H. Kobayashi, H. Sakaebe, K. Tatsumi, H. Kageyama, T. Nakamura, R. Kanno, *Journal of Materials Chemistry* **2003**, *13*, 7 1747.

[13] M. Yang, J. Jin, Y. Shen, S. Sun, X. Zhao, X. Shen, *ACS Applied Materials and Interfaces* **2019**, *11*, 47 44144.

[14] B. Li, M. T. Sougrati, G. Rousse, A. V. Morozov, R. Dedryvère, A. Iadecola, A. Senyshyn, L. Zhang, A. M. Abakumov, M.-L. Doublet, J.-M. Tarascon, *Nature Chemistry* **2021**, *13*, 11 1070.

[15] N. Yabuuchi, M. Takeuchi, S. Komaba, S. Ichikawa, T. Ozaki, T. Inamasu, *Chemical Communications* **2016**, *52*, 10 2051.

[16] D. A. Kitchaev, Z. Lun, W. D. Richards, H. Ji, R. J. Clément, M. Balasubramanian, D. H. Kwon, K. Dai, J. K. Papp, T. Lei, B. D. McCloskey, W. Yang, J. Lee, G. Ceder, *Energy Environmental Science* **2018**, *11*, 8 2159.

[17] C. Baur, I. Källquist, J. Chable, J. H. Chang, R. E. Johnsen, F. Ruiz-Zepeda, J.-M. Ateba Mba, A. J. Naylor, J. M. Garcia-Lastra, T. Vegge, F. Klein, A. R. Schür, P. Norby, K. Edström, M. Hahlin, M. Fichtner, *Journal of Materials Chemistry A* **2019**, *7*, 37 21244.

[18] B. Huang, R. Wang, Y. Gong, B. He, H. Wang, *Frontiers in Chemistry* **2019**, *7* 107.

[19] F. Geng, B. Hu, C. Li, C. Zhao, O. Lafon, J. Trébosc, J.-P. Amoureux, M. Shen, B. Hu, *Journal of Materials Chemistry* **2020**, *8*, 32 16515.

[20] J. Lee, D. A. Kitchaev, D.-H. Kwon, C.-W. Lee, J. K. Papp, Y.-S. Liu, Z. Lun, R. J. Clément, T. Shi, B. D. McCloskey, J. Guo, M. Balasubramanian, G. Ceder, *Nature* **2018**, *556*, 7700 185.

[21] S. Ahmed, P. A. Nelson, K. G. Gallagher, N. Susarla, D. W. Dees, *Journal of Power Sources* **2017**, *342* 733.

[22] Q. Dai, J. C. Kelly, L. Gaines, M. Wang, *Batteries* **2019**, *5*, 2 48.

[23] E. Emilsson, L. Dahllöf, Lithium-Ion Vehicle Battery Production Status 2019 on Energy Use, CO 2 Emissions, Use of Metals, Products Environmental Footprint, and Recycling, Technical report, **2019**, URL `www.ivl.se`.

[24] Z. Lun, B. Ouyang, D. A. Kitchaev, R. J. Clément, J. K. Papp, M. Balasubramanian, Y. Tian, T. Lei, T. Shi, B. D. McCloskey, J. Lee, G. Ceder, *Advanced Energy Materials* **2019**, *9*, 2 1802959.

[25] J. Ahn, D. Chen, G. Chen, *Advanced Energy Materials* **2020**, *10*, 35 2001671.

[26] Z. Lun, B. Ouyang, D. H. Kwon, Y. Ha, E. E. Foley, T. Y. Huang, Z. Cai, H. Kim, M. Balasubramanian, Y. Sun, J. Huang, Y. Tian, H. Kim, B. D. McCloskey, W. Yang, R. J. Clément, H. Ji, G. Ceder, *Nature Materials* **2020**, *20*, 2 214.

[27] Hyeseung Chung, Zachary Lebens-Higgins, Baharak Sayahpour, Carlos Mejia, Antonin Grenier, G. E. Kamm, Yixuan Li, Ricky Huang, L. F. J. Piper, K. W. Chapman, Jean-Marie Doux, Y. Shirley Meng, *Journal of Materials Chemistry A* **2021**, *9*, 3 1720.

[28] R. J. Clément, Z. Lun, G. Ceder, *Energy Environmental Science* **2020**, *13*, 2 345.

[29] Y. S. Moghadam, A. E. Kharbachi, T. Diemant, G. Melinte, Y. Hu, M. Fichtner, *Chemistry of Materials* **2021**, *33*, 21 8235.

[30] E. E. Levin, J. H. Grebenkemper, T. M. Pollock, R. Seshadri, *Chemistry of Materials* **2019**, *31*, 18 7151.

[31] M. B. Preefer, J. H. Grebenkemper, F. Schroeder, J. D. Bocarsly, K. Pilar, J. A. Cooley, W. Zhang, J. Hu, S. Misra, F. Seeler, K. Schierle-Arndt, R. Seshadri, *ACS Applied Materials Interfaces* **2019**, *11*, 45 42280.

[32] A. Urban, A. Abdellahi, S. Dacek, N. Artrith, G. Ceder, *Physical Review Letters* **2017**, *119*, 17 176402.

[33] S. Jouanneau, J. R. Dahn, *Journal of The Electrochemical Society* **2004**, *151*, 10 A1749.

[34] Z. Luo, W. Liu, G. Qu, A. Lu, G. Han, *Journal of Non-Crystalline Solids* **2014**, *388* 62.

[35] J. L. Santos, R. L. S. B. Marçal, P. R. R. Jesus, A. V. Gomes, E. P. Lima, S. N. Monteiro, J. B. de Campos, L. H. L. Louro, *Metallurgical and Materials Transactions A* **2017**, *48*, 10 4432.

[36] M. A. Jones, P. J. Reeves, I. D. Seymour, M. J. Cliffe, S. E. Dutton, C. P. Grey, *Chemical Communications* **2019**, *55*, 61 9027.

[37] Z. Cai, Y.-Q. Zhang, Z. Lun, B. Ouyang, L. C. Gallington, Y. Sun, H.-M. Hau, Y. Chen, M. C. Scott, G. Ceder, *Advanced Energy Materials* **2022**, *12*, 21 2103923.

[38] J. Li, N. Sharma, Z. Jiang, Y. Yang, F. Monaco, Z. Xu, D. Hou, D. Ratner, P. Pianetta, P. Cloetens, F. Lin, K. Zhao, Y. Liu, *Science* **2022**, *376*, 6592 517.

[39] B. M. Meyer, N. Leifer, S. Sakamoto, S. G. Greenbaum, C. P. Grey, *Electrochemical and Solid-State Letters* **2005**, *8*, 3 A145.

[40] B. Ouyang, N. Artrith, Z. Lun, Z. Jadidi, D. A. Kitchaev, H. Ji, A. Urban, G. Ceder, *Advanced Energy Materials* **2020**, *10*, 10 1903240.

[41] N. J. Szymanski, Y. Zeng, T. Bennett, S. Patil, J. K. Keum, E. C. Self, J. Bai, Z. Cai, R. Giovine, B. Ouyang, F. Wang, C. J. Bartel, R. J. Clément, W. Tong, J. Nanda, G. Ceder, *Chemistry of Materials* **2022**, *34*, 15 7015.

[42] D. Chen, W. H. Kan, G. Chen, *Advanced Energy Materials* **2019**, *9*, 31 1901255.

[43] Y. Yue, N. Li, L. Li, E. E. Foley, Y. Fu, V. S. Battaglia, R. J. Clément, C. Wang, W. Tong, *Chemistry of Materials* **2020**, *32*, 11 4490.

[44] Y. Zhang, E. C. Self, B. P. Thapaliya, R. Giovine, H. M. Meyer, L. Li, Y. Yue, D. Chen, W. Tong, G. Chen, C. Wang, R. Clément, S. Dai, J. Nanda, *ACS Applied Materials and Interfaces* **2021**, *13*, 32 38221.

[45] R. J. Clément, D. Kitchaev, J. Lee, Gerbrand Ceder, *Chemistry of Materials* **2018**, *30*, 19 6945.

[46] A. Coelho, *Journal of Applied Crystallography* **2018**, *51*, 1 210.

[47] B. H. Toby, R. B. Von Dreele, *Journal of Applied Crystallography* **2013**, *46*, 2 544.

[48] X. Yang, P. Juhas, C. L. Farrow, S. J. L. Billinge, X. Yang, P. Juhas, C. L. Farrow, S. J. L. Billinge, *arXiv* **2014**.

[49] C. L. Farrow, P. Juhas, J. W. Liu, D. Bryndin, E. S. Božin, J. Bloch, T. Proffen, S. J. L. Billinge, *Journal of Physics: Condensed Matter* **2007**, *19*, 33 335219.

[50] C. A. Schneider, W. S. Rasband, K. W. Eliceiri, *Nature Methods* **2012**, *9*, 7 671.

[51] D. Massiot, F. Fayon, M. Capron, I. King, S. Le Calvé, B. Alonso, J.-O. Durand, B. Bujoli, Z. Gan, G. Hoatson, *Magnetic Resonance in Chemistry* **2002**, *40*, 1 70.

[52] B. Ravel, M. Newville, *Journal of synchrotron radiation* **2005**, *12*, 4 537.